Research Article | Open Access

Microstructures

Dong *et al. Microstructures* **2026**, *6*, 2026095 **DOI:**10.20517/microstructures.2026.102

Eu^{3+}-doped GAGG scintillating transparent ceramics: optimization of optical, thermal, and X-ray imaging performance

Guangzhi Dong[1,2], Xiaorong Yang[1], Chaoke Lv[1], Rulang Bai[1], Huanhuan Su[1], Bilin Zhang[1], Xiaowang Liu[3], Tao Wang[4], Wanqi Jie[4]

Keywords:
GAGG: xEu^{3+}, transparent ceramics, scintillator, X-ray imaging

Citation: Dong, G.; Yang, X.; Lv, C.; Bai, R.; Su, H.; Zhang, B.; Liu, X.; Wang, T.; Jie, W. Eu^{3+}-doped GAGG scintillating transparent ceramics: optimization of optical, thermal, and X-ray imaging performance. *Microstructures* **2026**, *6*, 2026095. https://dx.doi.org/10.20517/microstructures.2026.102

Received: 19 May 2026 **First Decision:** 22 May 2026 **Revised:** 22 Jun 2026 **Accepted:** 26 Jun 2026 **Published:** 9 Jul 2026

Academic Editor: Dawei Wang **Copy Editor:** Ping Zhang **Production Editor:** Ping Zhang

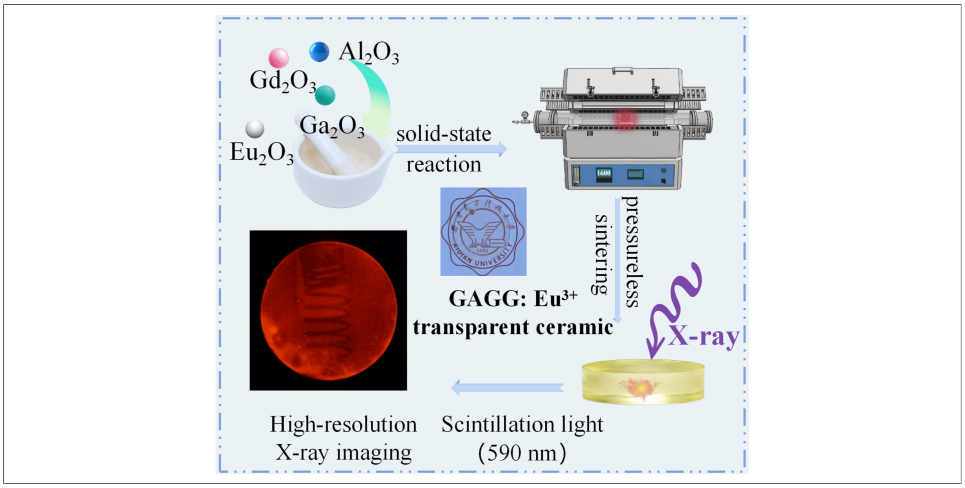

Abstract

Scintillators, which are critical for X-ray detection, are widely used in medical imaging, radiation detection, and high-energy physics. In this study, Eu^{3+}-doped $Gd_3Al_3Ga_2O_{12}$ (GAGG: xEu^{3+}) transparent ceramic scintillators were fabricated using a solid-state reaction method combined with pressureless atmosphere sintering. The effect of Eu^{3+} concentration on the optical quality, scintillation performance, and thermal stability of the ceramics was systematically investigated, and their X-ray imaging performance was preliminarily evaluated. The as-prepared ceramics exhibited high optical transmittance and a uniform grain-size distribution. Photoluminescence (PL) spectra revealed characteristic Eu^{3+} emission peaks at approximately 590 nm, corresponding to the dominant $^5D_0 \rightarrow {}^7F_1$ magnetic dipole transition. The optimal Eu^{3+} concentration was determined to be 2 at%, and the concentration quenching behavior was predominantly governed by electric dipole-dipole interactions. Furthermore, the GAGG: xEu^{3+} ceramics demonstrated satisfactory thermal stability and radioluminescence performance, with the radioluminescence intensity

[1]School of Advanced Materials and Nanotechnology, Xidian University, Xi'an 710126, Shannxi, China.
[2]School of Mechanical Engineering, Xi'an Jiaotong University, Xi'an 710049, Shannxi, China.
[3]Institute of Flexible Electronics, Northwestern Polytechnical University, Xi'an 710072, Shannxi, China.
[4]School of Materials Science and Engineering, Northwestern Polytechnical University, Xi'an 710072, Shannxi, China.

Correspondence to: Assoc. Prof. Guangzhi Dong, School of Advanced Materials and Nanotechnology, Xidian University, Xi'an 710126, Shannxi, China. E-mail: gzdong@xidian.edu.cn

reaching its maximum at a doping concentration of 3 at%. The discrepancy between the optimal concentrations obtained from PL and radioluminescence measurements is attributed to the different excitation mechanisms involved. These results indicate that GAGG: xEu^{3+} transparent ceramics are promising candidates for X-ray detection and imaging applications.

INTRODUCTION

Scintillators are functional materials capable of converting high-energy particles or radiation into detectable ultraviolet or visible light[1]. Owing to this unique property, they are widely used in medical imaging, radiation detection, and national security applications[2,3]. During X-ray detection, scintillators absorb incident high-energy radiation and become excited, subsequently emitting fluorescence. The emitted fluorescence is then converted into electrical signals by photodetectors, such as photomultiplier tubes (PMTs), photodiode arrays, and charge-coupled device/complementary metal-oxide-semiconductor (CCD/CMOS) detectors, thereby transforming otherwise invisible high-energy radiation into displayable signals or images for further analysis[4]. Therefore, scintillators play a crucial role in X-ray detection systems.

Garnet-type scintillation materials have attracted considerable attention owing to their excellent optical transparency, compositional flexibility, and tunable luminescence properties[5]. $Gd_3Al_3Ga_2O_{12}$ (GAGG)-based ceramics, which belong to the cubic garnet crystal system, are particularly promising for X-ray detection due to their high density (~6.7 g·cm^{-3}), large effective atomic number (Z_{eff} = 55), strong absorption capability for high-energy photons, and high light yield[6].

Research on GAGG-based materials began with single-crystal forms. Kuwano *et al.*[7] first grew GAGG: Nd single crystals and demonstrated their potential for laser materials. Kamada *et al.*[8,9] successfully fabricated 2-inch GAGG: Ce single crystals using the micro-pulling-down and Czochralski methods. These crystals exhibited an emission wavelength of approximately 520 nm and a density of 6.63 g·cm^{-3}, highlighting their potential for high-energy radiation detection applications, including medical computed tomography (CT) and security screening. Kunikata *et al.*[10] systematically investigated the influence of Eu^{3+} concentration on the optical and scintillation properties of $Gd_3Al_2Ga_3O_{12}$ single crystals, observing the characteristic 4f-4f transitions of Eu^{3+} and their millisecond-scale decay behavior. Endo *et al.*[11] improved the light yield of Eu: GAGG single crystals through optimization of the Al/Ga ratio. Despite their excellent scintillation performance, single-crystal materials suffer from several inherent limitations, including long growth cycles, high production costs, and restrictions on crystal size and dopant concentration, which significantly hinder their large-scale application[12].

To overcome the limitations associated with single crystals, GAGG-based ceramics have attracted increasing attention owing to their shorter fabrication cycles, lower production costs, ability to achieve homogeneous high-concentration doping, and suitability for large-scale manufacturing[13]. Kanai *et al.*[6] were the first to synthesize GAGG: Ce ceramics via a solid-state reaction method and investigated the effect of compositional deviation on afterglow, although the resulting samples exhibited poor optical quality. Seeley *et al.*[14] prepared a series of GYGAG: Ce ceramics and systematically examined the effects of calcination and sintering atmospheres on their scintillation performance. Yanagida *et al.*[15] fabricated GAGG: Ce ceramics with a thickness of 1 mm and a doping concentration of 1 at%, achieving scintillation performance that partially exceeded that of single crystal counterparts, although the optical transmittance remained low. Wu *et al.*[16] compared the scintillation properties of Ce: $(Lu,Gd)_3(Ga,Al)_5O_{12}$ ceramics and GAGG: Ce single crystals. The results showed that ceramics exhibited a higher light output (48,200 Ph/MeV) than single crystals (45,000 Ph/MeV), further demonstrating the considerable potential of GAGG-based ceramics for scintillation applications.

Studies have demonstrated that incorporation of rare-earth ions (RE^{3+}) into host lattices can effectively tailor their optical and electronic properties, thereby broadening their functional applications[17,18]. Liu *et al.*[19,20] prepared GAGG: Ce ceramics with a luminous efficiency of 388 $lm \cdot W^{-1}$, making them suitable for high-power blue LED devices. Dimitrakopoulos *et al.*[21] demonstrated that GAGG:Ce materials exhibit excellent stability and efficiency under medical X-ray irradiation, highlighting their potential for X-ray imaging devices. Among various rare-earth activators, Eu^{3+} has attracted considerable attention as an efficient red-emitting luminescence center owing to its unique 4f electronic configuration and outstanding red emission characteristics[22,23]. Xu *et al.*[24] fabricated GAGG: Cr^{3+}/Eu^{3+} transparent ceramics and achieved broadband continuous emission centered at 730 nm, demonstrating their potential for bioimaging applications. In addition, the narrow-band emission peaks of Eu^{3+} ions within the 550-750 nm range exhibit excellent spectral matching with silicon photodiodes, which are widely used in radiation detection systems[13]. Therefore, GAGG: Eu^{3+} ceramics hold significant application prospects in the high-energy field[25]. However, studies on Eu^{3+}-doped GAGG ceramics remain limited, and the luminescence mechanisms and thermal stability of this system have not yet been fully understood, warranting further investigation.

In this study, GAGG: $x$$Eu^{3+}$ (x = 1~4 at%) transparent ceramics were fabricated via an optimized solid-state reaction route followed by pressureless sintering. The effects of Eu^{3+} content on the optical transmittance, photoluminescence, and scintillation properties of the ceramics were systematically investigated. In addition, the luminescence thermal stability and defect-related characteristics were comprehensively analyzed through temperature-dependent emission spectroscopy and thermoluminescence measurements. Based on their excellent optical quality, the radioluminescence behavior and potential applicability of GAGG: Eu^{3+} ceramics in X-ray imaging were also evaluated.

MATERIALS AND METHODS

$(Eu_xGd_{1-x})_3Al_3Ga_2O_{12}$ scintillation ceramics (abbreviated as GAGG: $x$$Eu^{3+}$, x = 1, 2, 3, 4 at%) were fabricated using a solid-state reaction method combined with pressureless sintering. High-purity raw oxides, including gadolinium oxide (Gd_2O_3, 99.9%, Macklin), alumina (Al_2O_3, 99.9%, Aladdin), gallium oxide (Ga_2O_3, 99.99%, Aladdin), and europium oxide (Eu_2O_3, 99.9%, Aladdin), were accurately weighed as starting materials. The raw materials were milled in a planetary ball mill for 12 h. After drying the slurry at 80 °C, the resulting powder was sieved through a 200-mesh screen. The sieved powder was subsequently compacted into pellets by uniaxial pressing and further densified via cold isostatic pressing at 250 MPa. The obtained green body was then calcined at 1,000~1,300 °C for 4 h in an air atmosphere. After calcination, the samples were sintered at 1,600~1,620 °C for 10 h in an oxygen atmosphere to obtain dense ceramics.

The phase composition of the samples was analyzed by X-ray powder diffraction (XRD, D8 Advance, Bruker, Germany). The microstructural and elemental distribution were examined using transmission electron microscopy (TEM, F200X, Thermo Fisher Scientific, USA) and scanning electron microscopy (SEM, JSM-7500F, JEOL, Japan). The optical transmittance spectra were measured using an ultraviolet-visible-near-infrared (UV-Vis-NIR) spectrophotometer (Lambda950, PerkinElmer, USA). Photoluminescence excitation (PLE) and photoluminescence (PL) spectra were recorded using a fluorescence spectrometer (FLS-1000, Edinburgh Instruments, UK). Radioluminescence spectra were obtained using an X-ray excitation and emission spectrometer (XEL, OmniFLUO990-Xray, Zhuoli, China). The defect states of the ceramics were evaluated using thermally stimulated luminescence (TSL) measurements using a three-dimensional thermoluminescence spectrometer (TOSL-3DS, Radiation Technology, China).

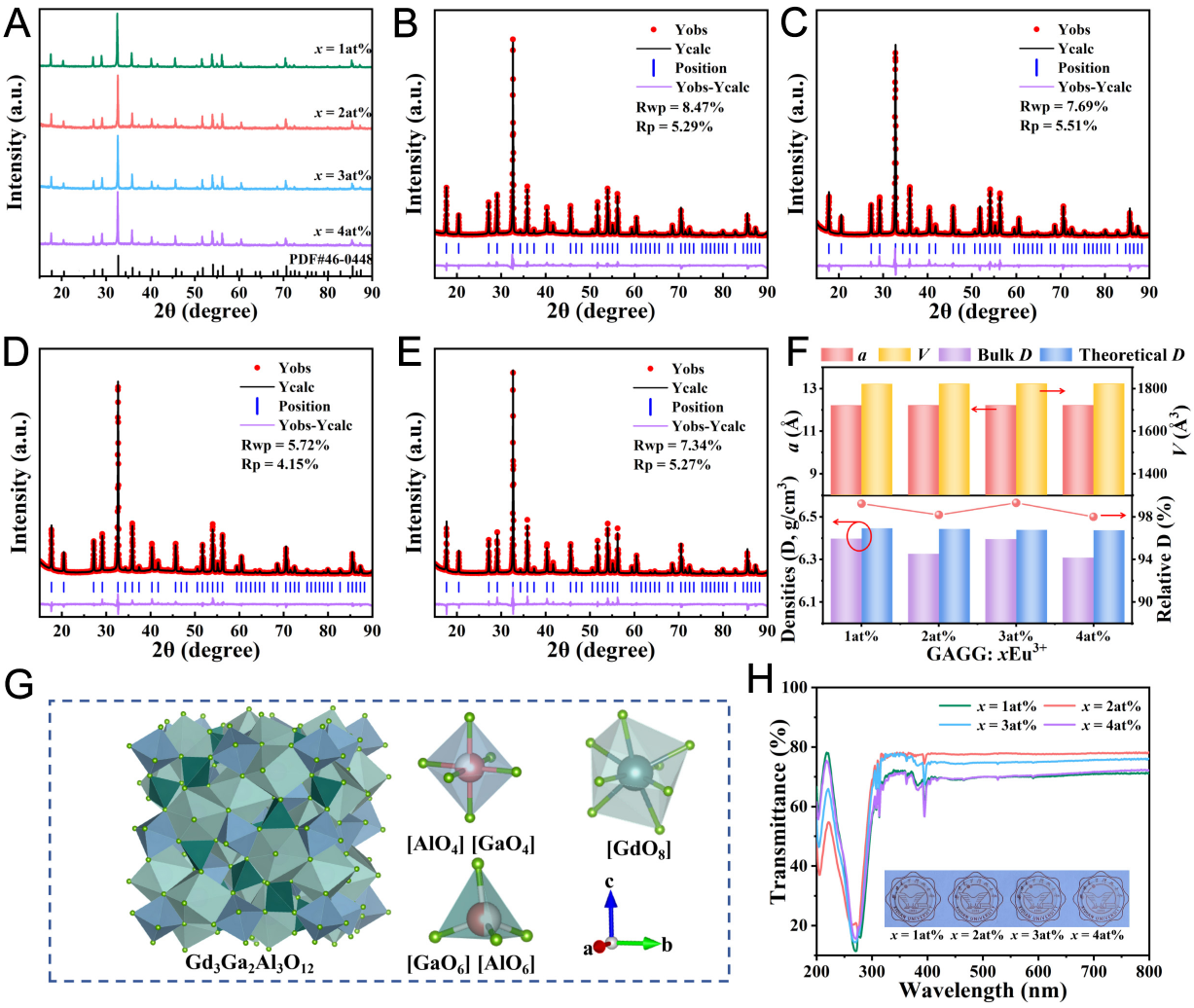

Figure 1. (A) XRD patterns, (B-E) Rietveld refinement results, (F) lattice parameters and densities, (G) schematic crystal structure, (H) optical transmittance spectra and photographs (inset) of GAGG: xEu^{3+} (x = 1~4 at%) ceramics. GAGG: $Gd_3Al_3Ga_2O_{12}$.

RESULTS AND DISCUSSION

Phase and morphology analysis

The XRD patterns of the GAGG: xEu^{3+} transparent ceramics, shown in Figure 1A, confirm that all diffraction peaks can be well indexed to the standard $Gd_3Al_3Ga_2O_{12}$ (PDF#46-0448), with no detectable secondary phases. This result indicates that the incorporation of Eu^{3+} ions does not alter the garnet crystal structure of the host lattice. To further verify the phase purity and structural characteristics, Rietveld refinements were performed using GSAS-Ⅱ software[26]. The corresponding refinement profiles are presented in Figure 1B-E. The obtained reliability factors (R_{wp} = 5.72%~8.47%) demonstrate satisfactory fitting quality. The refined structural parameters are summarized in Figure 1F and Table 1. As the Eu^{3+} concentration increases, both the lattice constant and unit-cell volume exhibit a slight increase, suggesting that Eu^{3+} ions are successfully incorporated into the lattice through substitution at the Gd^{3+} sites. The bulk densities (D) of GAGG: xEu^{3+} ceramics, measured by the Archimedes method, are approximately 6.4 g·cm^{-3}, corresponding to more than 98% of the theoretical density. These results indicate that highly densified ceramics were successfully obtained.

The schematic illustration of the GAGG crystal structure is presented in Figure 1G. GAGG crystallizes in a cubic garnet structure with space group O_h^{10}-$Ia3d$. In this structure, Gd^{3+} ions occupy the dodecahedral

Table 1. Lattice and refinement parameters of GAGG: *x*Eu^{3+} ceramics

Parameters	*x* = 1 at%	*x* = 2 at%	*x* = 3 at%	*x* = 4 at%
R_p (%)	5.29	5.51	4.15	5.27
R_{wp} (%)	8.47	7.69	5.72	7.34
$a = b = c$ (Å)	12.213	12.214	12.215	12.216
V (Å^3)	1,821.659	1,822.106	1,822.554	1,823.002
Density (g·cm^{-3})	6.446	6.443	6.439	6.437

GAGG: $Gd_3Al_3Ga_2O_{12}$.

[GdO_8] sites coordinated by eight O^{2-} ions, whereas Ga^{3+} and Al^{3+} preferentially occupy the octahedral [GaO_6] and tetrahedral [AlO_4] sites, respectively. However, partial cation disorder between Ga^{3+} and Al^{3+} ions may occur, resulting in the coexistence of [AlO_6] octahedra and [GaO_4] tetrahedra[6]. Additionally, Gd^{3+} ions at dodecahedral sites can be readily substituted by rare earth ions with similar ionic radii, thereby facilitating the luminescence of diverse rare earth activators[27,28]. The ionic radii of Eu^{3+} and Gd^{3+} are 0.0947 and 0.0938 nm, respectively. The slightly larger radius of Eu^{3+} facilitates its incorporation into the GAGG lattice via Gd^{3+}, promoting efficient luminescence activation within the solid solution.

As shown in Figure 1H, the polished GAGG: *x*Eu^{3+} transparent ceramics (thickness = 1 mm) exhibit excellent transparency without visible defects, confirming good optical quality. The prepared ceramics demonstrate optical transmittance values of approximately 70% within the 400-800 nm range. Among the investigated samples, the ceramic doped with the 2 at% Eu^{3+} exhibits the highest value of 77%, which is comparable to that reported for GAGG single crystals. Several sharp absorption peaks are observed in the visible region around 394, 466, and 527 nm, which correspond to Eu^{3+}-related 4f-4f transitions[29].

To further investigate the influence of Eu^{3+} doping on the microstructural evolution of GAGG ceramics, polished samples were thermally etched at 1,300 °C in air. The resulting SEM micrographs are shown in Figure 2. All samples exhibit dense microstructures with well-defined grain boundaries, and no obvious pores or secondary phases are observed. These results indicate a high degree of densification, which is consistent with the XRD and density measurements discussed above. To quantitatively evaluate the microstructural characteristics, grain-size distributions were analyzed, as in the inset of Figure 2. The average grain size shows a non-monotonic dependence on the Eu^{3+} concentration, increasing initially and then decreasing. The maximum average grain size of 8.32 μm occurs at 2 at% Eu^{3+}, which also exhibits the highest optical transmittance. This enhancement is attributed to reduced light scattering at grain boundaries due to grain growth, effectively lowering optical losses and improving transparency in the ceramics.

The microstructure of the optimal GAGG: 2 at% Eu^{3+} ceramic was further characterized by TEM. The selected area electron diffraction (SAED) pattern shown in Figure 3A exhibits well-defined diffraction spots along the [211] zone axis, indicating the high crystallinity of the GAGG phase.

The high-angle annular dark-field scanning transmission electron microscopy (HAADF-STEM) image acquired along the [211] direction is presented in Figure 3B. Clear lattice fringes can be observed, demonstrating the excellent crystallinity of the ceramic. The measured interplanar spacing is 0.87 nm, corresponding to the $(00\bar{1})$ plane, which agrees well with the theoretical value of 0.86 nm (PDF#46-0448). To evaluate the elemental distribution within the ceramic, energy dispersive spectroscopy (EDS) mapping was performed on a representative region, as shown in Figure 3C. The results indicate that Gd, Al, Ga, Eu, and O elements are uniformly distributed, with no other impurity elements detected. Additionally, no obvious elemental segregation or enrichment phenomenon is observed. Combining the

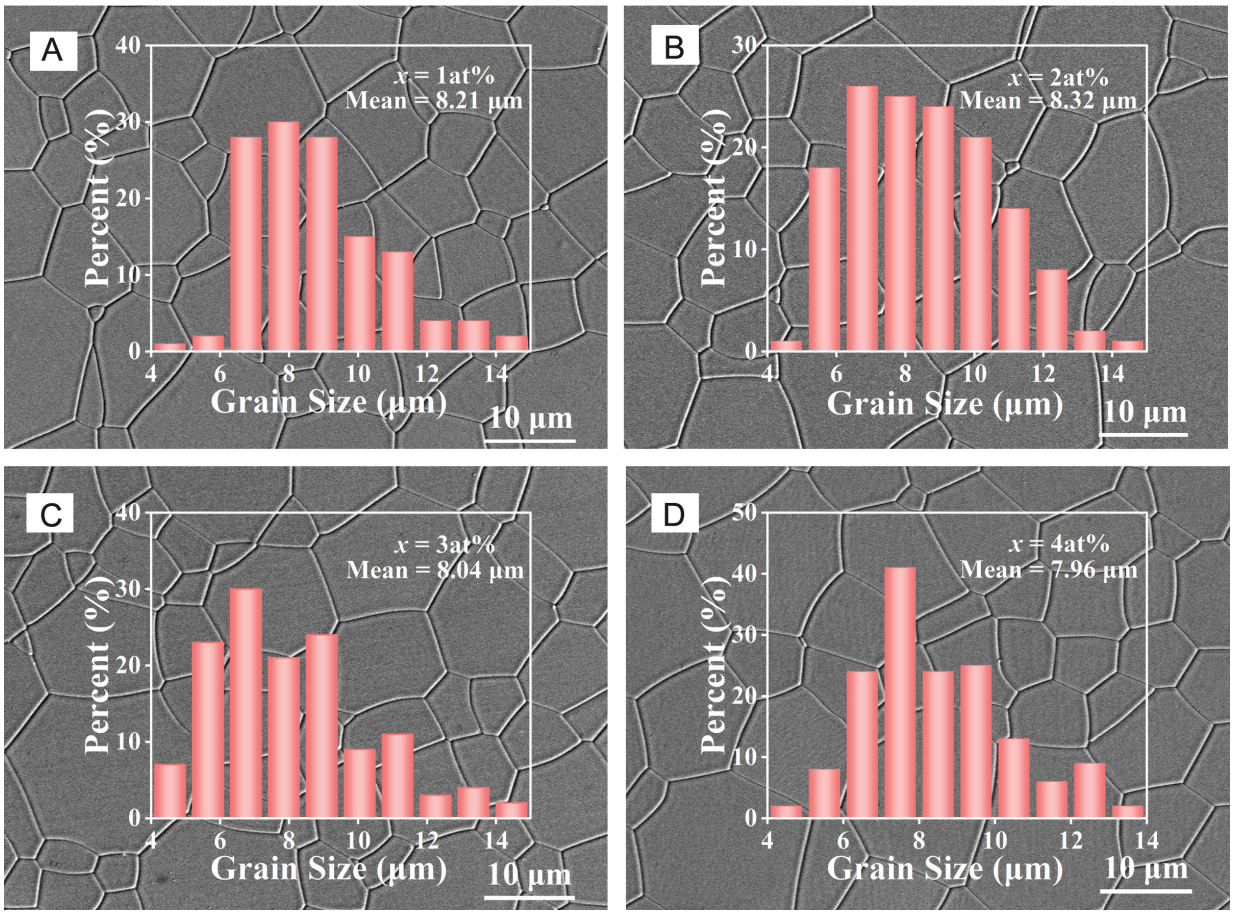

Figure 2. SEM images and grain size distributions of GAGG: xEu^{3+} transparent ceramics. GAGG: $Gd_3Al_3Ga_2O_{12}$; SEM: scanning electron microscopy.

TEM and EDS analysis results, it is confirmed that the prepared ceramics possess high uniformity and optical quality.

Optical properties

The PLE spectrum of the GAGG: 2 at% Eu^{3+} ceramic is shown in Figure 4A. Five distinct excitation bands are observed in 350-500 nm, which can be assigned to the following intra-4f transitions of Eu^{3+} ions: $^7F_0 \rightarrow {}^5D_4$, $^7F_0 \rightarrow {}^5L_7$, $^7F_0 \rightarrow {}^5L_6$, $^7F_0 \rightarrow {}^5D_3$, and $^7F_0 \rightarrow {}^5D_2$ [30]. The PL spectra of GAGG: xEu^{3+} ceramics with different Eu^{3+} concentrations are presented in Figure 4B. A dominant orange-red peak is observed at 590 nm, corresponding to the $^5D_0 \rightarrow {}^7F_1$ magnetic dipole transition of Eu^{3+} ions. Additional emission peaks located at 610 and 630 nm are attributed to the $^5D_0 \rightarrow {}^7F_2$ electric dipole transition, while the weaker emission bands at 653, 695, and 710 nm originate from the $^5D_0 \rightarrow {}^7F_3$ and $^5D_0 \rightarrow {}^7F_4$ transitions, respectively[31]. Based on the Eu^{3+} emission spectrum, a schematic energy-level diagram illustrating the photoluminescence process is proposed, as shown in Figure 4C.

Studies have shown that the luminescence behavior of Eu^{3+} ions is highly sensitive to their local crystal environment. In the PL spectrum, the $^5D_0 \rightarrow {}^7F_1$ magnetic dipole transition remains dominant, indicating that Eu^{3+} ions occupy sites with relatively high symmetry in the host lattice[32] The emission intensity initially increases with increasing Eu^{3+} concentration and reaches a maximum at 2 at%, beyond which concentration quenching becomes apparent. This quenching behavior is likely associated with reduced interionic distance between Eu^{3+} ions at higher doping concentrations, which facilitates energy transfer among activator ions

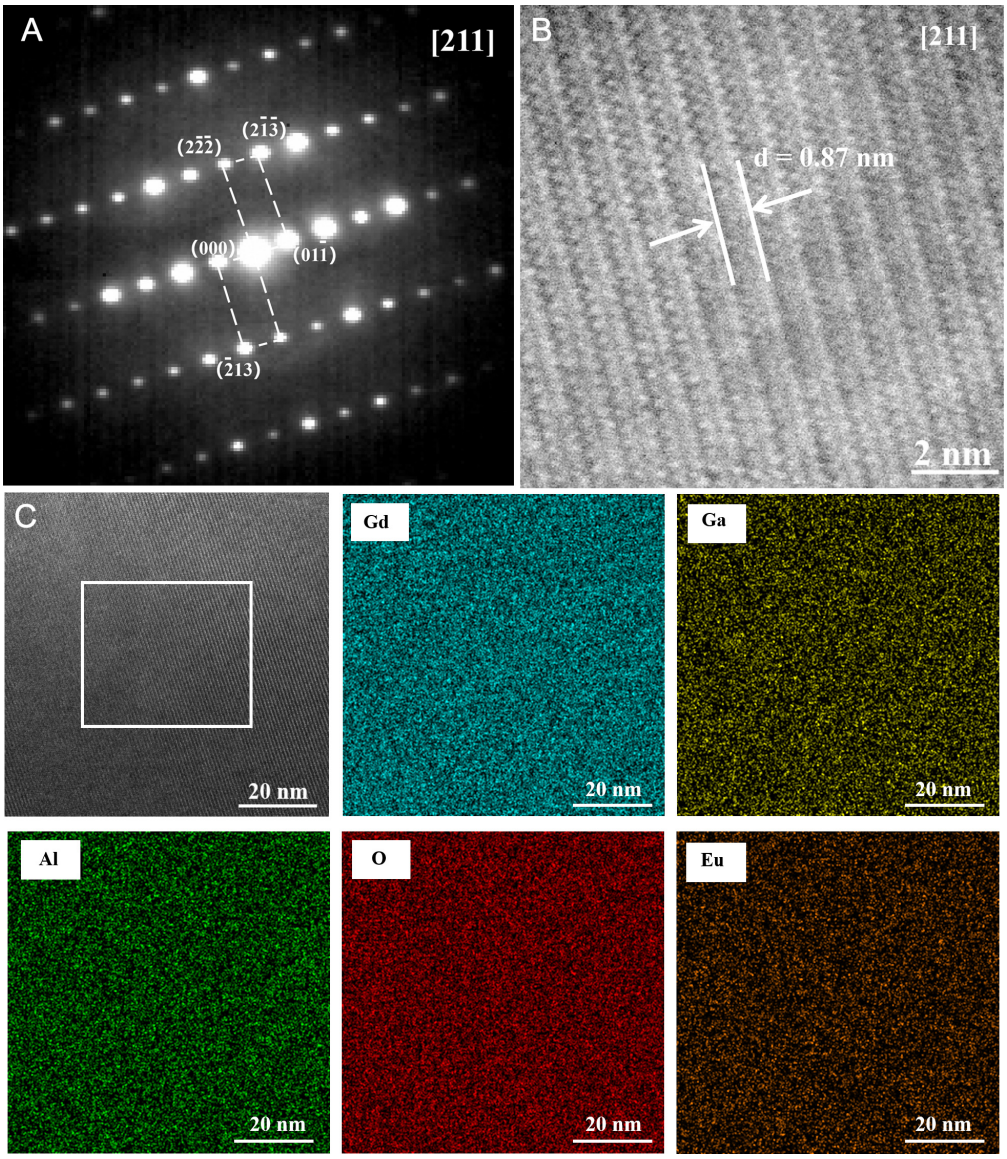

Figure 3. TEM characterization of GAGG: 2 at% Eu^{3+} ceramic: (A) SAED pattern, (B) HAADF-STEM image, and (C) EDS elemental mapping. GAGG: $Gd_3Al_3Ga_2O_{12}$; TEM: transmission electron microscopy; HAADF-STEM: high-angle annular dark-field scanning transmission electron microscopy; SAED: selected area electron diffraction; EDS: energy dispersive spectroscopy.

and increases the probability of excitation energy being trapped by defect states or impurity levels. The trapped energy may subsequently be dissipated through non-radiative relaxation or transferred to impurity ions, thereby reducing the luminescence efficiency of Eu^{3+} ions[33,34]. The non-radiative energy transfer between rare earth ions can occur through two primary mechanisms: exchange interaction and electric multipole interaction[35]. According to the Blasse model[36], the critical distance (R_c) for doped ions can be calculated using Equation (1):

$$R_c = 2\left(\frac{3V}{4\pi X_c N}\right)^{\frac{1}{3}} \quad (1)$$

Where (X_c) is the critical doping concentration; (V) is the unit-cell volume and (N) represents the number of available substitutional sites per unit cell. For the GAGG ceramics, $a = b = c = 12.214$ Å, $N = 8$, and $V = abc = 1{,}822.106$ Å^3, the calculated (R_c) is 22.15 Å. When $R_c < 5$ Å, energy transfer is predominantly governed by exchange interaction. The calculated (R_c) is significantly larger than 5 Å, indicating that the concentration quenching behavior is primarily attributed to electric multipolar interaction rather than exchange

interaction[37]. To further clarify the electric multipolar interaction mechanism, Dexter's theory[38] was employed to analyze the relationship between the luminescence intensity (I) and the Eu^{3+} concentration (x), which can be expressed by Equation (2):

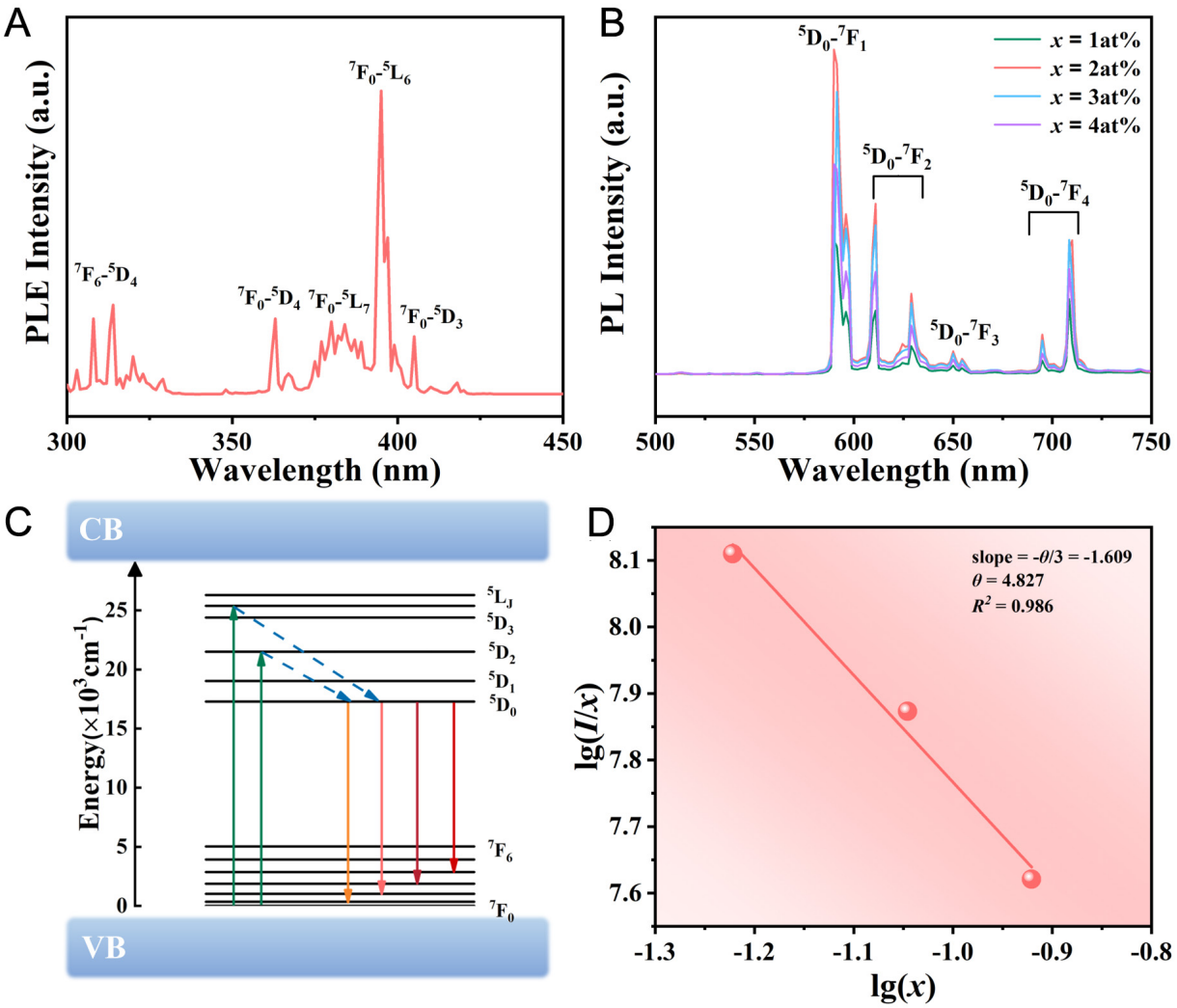

Figure 4. (A) PLE spectrum of GAGG: 2at% Eu^{3+} ceramic; (B) Emission spectra of GAGG: xEu^{3+}; (C) Schematic diagram of the Eu^{3+} photoluminescence energy-level transitions; (D) Relationship between lg(I/x) and lg(x) for GAGG: xEu^{3+} ceramics. GAGG: $Gd_3Al_3Ga_2O_{12}$; PLE: photoluminescence excitation.

$$lg(I/x) = C - (\theta/3)lgx \quad (2)$$

where (I) represents the luminous intensity of the $^5D_0 \rightarrow {}^7F_1$ transition, while (C) and (θ) are constants. The type of multipolar interaction can be identified according to the value of (θ), where θ = 6, 8, and 10 correspond to electric dipole-electric dipole (d-d), electric dipole-electric quadrupole (d-q), and electric quadrupole-electric quadrupole (q-q), respectively[39]. The plot of $lg(I/x)$ versus $lg(x)$ is shown in Figure 4D, where the slope is equal to -θ/3. From this plot, the value of θ was calculated to be approximately 4.827, which is close to 6. This result indicates that the concentration quenching mechanism in GAGG: xEu^{3+} is governed by electric dipole-dipole interactions[40].

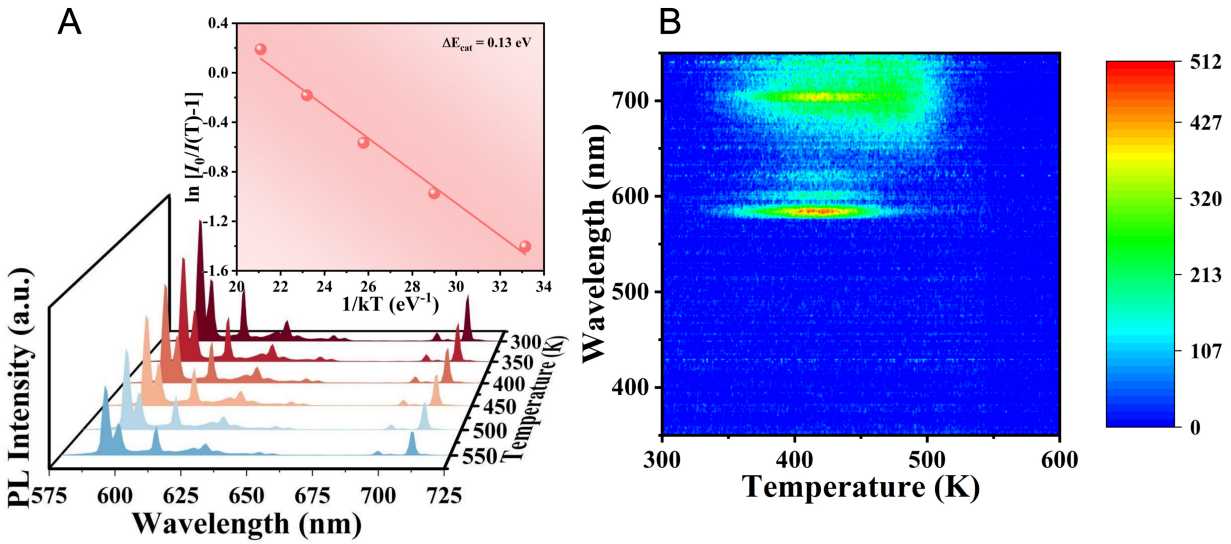

Figure 5. GAGG: 2at% Eu^{3+} ceramic: (A) Temperature-dependent PL spectra, and the Arrhenius relationship between $\ln[I_0/I(T)-1]$ and $1/kT$; (B) Thermally stimulated luminescence spectra. GAGG: $Gd_3Al_3Ga_2O_{12}$; PL: photoluminescence.

To evaluate the luminescence stability of GAGG: xEu^{3+} ceramics, temperature-dependent PL spectra of the GAGG: 2 at% Eu^{3+} sample were recorded over the temperature range of 300~550 K, as shown in Figure 5A. The luminescence intensity of Eu^{3+} gradually decreases with increasing temperature and retains 50.28% of its initial intensity when the temperature reaches 550 K. The decrease in luminescence intensity with increasing temperature is attributed to thermal quenching. As the temperature rises, electrons in the excited states of the luminescence centers can be thermally activated to higher vibrational levels and subsequently return to the ground state through non-radiative relaxation processes, leading to a reduction in luminescence intensity[41]. The thermal quenching is closely related to the strength of phonon-electron coupling[42]. The activation energy (ΔE_a) for thermal quenching was calculated by fitting the temperature-dependent luminescence intensity using the Arrhenius[43] Equation (3):

$$I(T) = I_0/[1 + Bexp\,(-\Delta E_a/kT)] \quad (3)$$

where (I_0) is the initial luminescence intensity, $I(T)$ is the luminescence intensity at a given temperature; (B) is a constant and (k) is the Boltzmann constant. The fitted curve for ΔE_a across the temperature range of 300-550 K is shown in the inset of Figure 5A. The fitting process yields ΔE_a = 0.13 eV. A higher ΔE_a indicates enhanced stability, as it corresponds to a higher non-radiative energy barrier that must be overcome during the transition from the excited state to the ground state. This elevated barrier effectively suppresses nonradiative relaxation, thereby confirming the excellent thermal stability of the GAGG: 2 at% Eu^{3+} ceramic[44].

To further examine the influence of defect states on the thermal stability of radioluminescence in ceramics, TSL measurements were performed on the 2 at% Eu^{3+} ceramic, and the corresponding spectra are presented in Figure 5B. Unlike the sharp Eu^{3+} emission lines observed in the PL spectra, the TSL spectrum exhibits a broad red emission band in the 650-750 nm range, indicating that TSL process does not simply follow the PL emission mechanism. During TSL measurements, thermally released charge carriers undergo recombination through defect-related or activator-related radiative pathways. Therefore, the broad emission band centered at approximately 700 nm is likely associated with defect-mediated recombination processes within the GAGG lattice, involving oxygen vacancies, antisite defects, and local lattice distortions, together with a

possible contribution from the weak Eu^{3+} $^5D_0 \rightarrow {}^7F_4$ transition. Continuous trap distributions are observed over the temperature range of 340~550 K. This is likely due to the stronger lattice vibrations at higher temperatures, which cause the release of electrons (or holes) from traps, leading to light emission. Their release difficulty depends on both the depth of the trap and the temperature of the material. Shallow trap levels can release charge carriers at relatively low temperatures, whereas deep trap levels require higher temperatures for carrier release. The relationship between the temperature and the trap depth (E) can be calculated using Equation (4)[45]:

$$E = \left(0.94 \ln \frac{s}{\beta} + 4.12\right) \times kTm \tag{4}$$

where (Tm) is the temperature corresponding to the TSL peak, (s) is the frequency factor, (β) is the heating rate, and (k) is the Boltzmann constant. In this measurement, (β) was fixed at 1 °C/s. Considering that the frequency factor (s) typically falls within the range of 10^{10}~10^{14}, a characteristic value of 10^{12} was adopted to simplify the calculation while maintaining reasonable accuracy. The calculated trap depths of the GAGG: 2 at% Eu^{3+} ceramic range from 1.62 eV to 1.85 eV, indicating the presence of medium and deep trap levels. Generally, shallow traps can release charge carriers at relatively low temperatures and may participate in rapid carrier recombination processes. However, an excess concentration of shallow traps can increase the probability of non-radiative recombination, thereby reducing luminescence efficiency. In contrast, deeper traps require higher thermal energy for carrier release and can temporarily store charge carriers during excitation. These traps are beneficial for regulating carrier capture and delayed release processes, thereby influencing the thermal stability and radioluminescence performance of the material[46].

Scintillation properties

To evaluate the high-energy X-ray detection capability of GAGG: $x$$Eu^{3+}$ transparent ceramics, as shown in Figure 6A. The GAGG: Eu ceramics exhibit X-ray absorption capability comparable to that of commercial scintillators. The scintillation properties were further characterized by X-ray-excited emission spectroscopy, and the corresponding spectra for different Eu^{3+} concentrations are presented in Figure 6B. The radioluminescence spectra are generally consistent with the PL spectra. Among the prepared GAGG: $x$$Eu^{3+}$ ceramics, the highest luminescence intensity is observed at 3 at%. When the Eu^{3+} concentration exceeds this value, concentration quenching becomes apparent. The quenching phenomenon observed under X-ray excitation differs from that observed in the PL spectra. The discrepancy in the optimal Eu^{3+} concentration between PL and X-ray-excited luminescence can be attributed to the different excitation and energy-transfer pathways. Under UV excitation, Eu^{3+} ions are mainly excited through localized 4f-4f transitions, and the emission intensity is strongly influenced by concentration-dependent energy migration among Eu^{3+} ions. In contrast, under X-ray excitation, the scintillation process involves X-ray absorption by the host lattice, generation of secondary electrons and holes, carrier transport, defect trapping and release, and subsequent energy transfer to Eu^{3+} emission centers. Therefore, the scintillation performance is jointly influenced by Eu^{3+} concentration, defect states, and optical transparency[39]. The CIE 1931 chromaticity coordinates derived from X-ray-excited emission spectra are shown in Figure 6C. All GAGG: $x$$Eu^{3+}$ ceramics exhibit red emission in the visible region, indicating their potential for optoelectronic applications.

In addition, the dependence of the radioluminescence intensity of the GAGG: 2 at% Eu^{3+} ceramic on X-ray tube power was investigated, as shown in Figure 6D. The results show that the luminescence intensity increases steadily with increasing X-ray power. This enhancement is attributed to the increased flux of incident X-ray photons at higher power levels. These photons interact with the scintillator through processes such as the photoelectric effect and Compton scattering, generating a larger number of secondary electrons. The generated secondary electrons subsequently transfer energy to the luminescent centers, resulting in

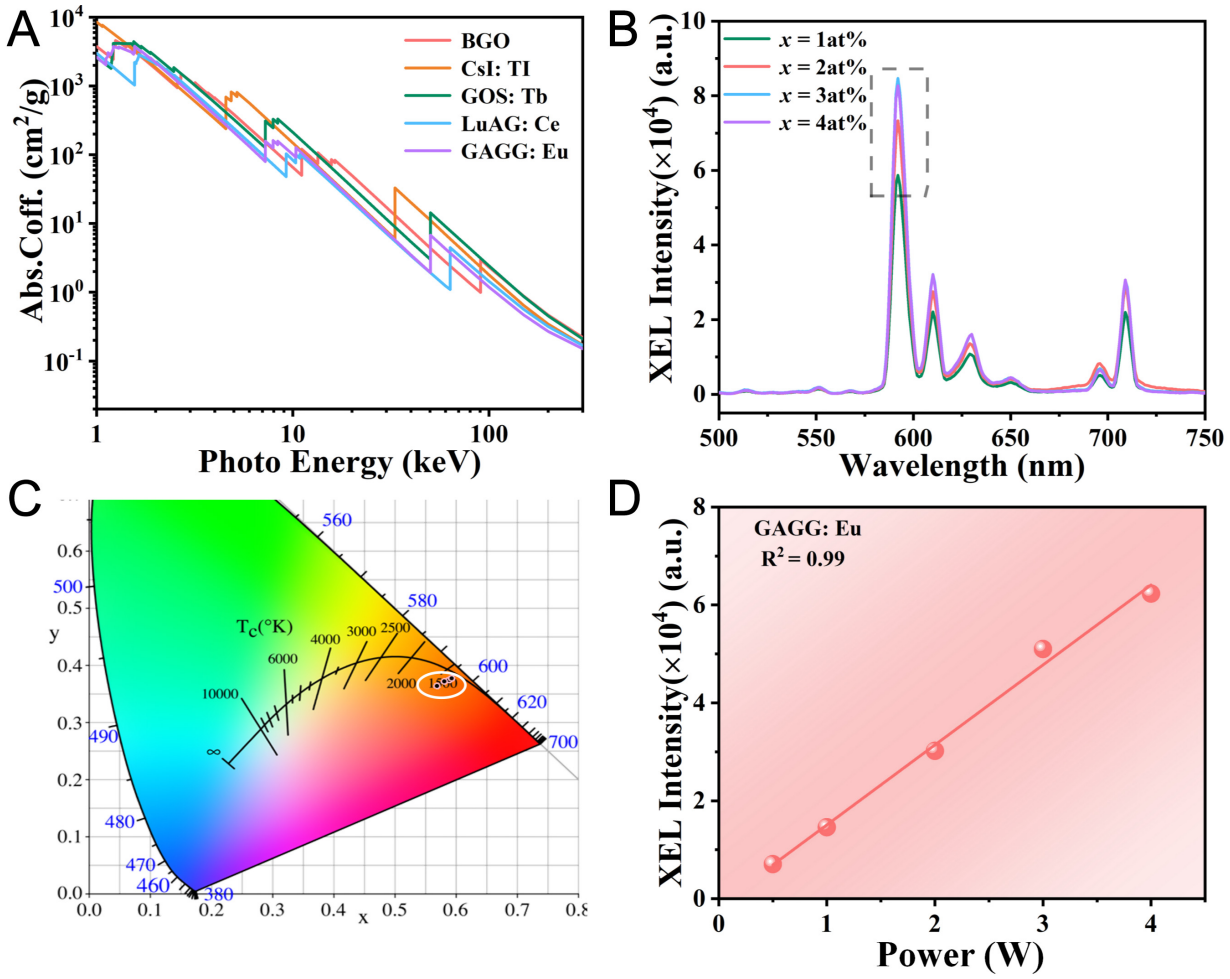

Figure 6. (A) Comparison of X-ray absorption coefficients among BGO, CsI: Tl, GOS: Tb, LuAG: Ce and GAGG: Eu^{3+}; (B) X-ray-excited emission spectra, and (C) CIE chromaticity coordinates of GAGG: xEu^{3+} transparent ceramics; (D) Relationship between X-ray power and luminescence intensity of GAGG: 2at% Eu^{3+} ceramic. GAGG: $Gd_3Al_3Ga_2O_{12}$; CIE: International Commission on Illumination; XEL: X-ray excited luminescence; BGO: $Bi_4Ge_3O_{12}$, Bismuth Germanate; CsI:Tl: thallium-doped cesium iodide; GOS:Tb: Gd_2O_2S:Tb, terbium-doped gadolinium oxysulfide; LuAG:Ce: $Lu_3Al_5O_{12}$:Ce, cerium-doped lutetium aluminum garnet.

enhanced visible light emission. These findings suggest that the prepared ceramic scintillator holds promise for applications in X-ray detection.

To explore the potential of the prepared GAGG: xEu^{3+} transparent ceramics as scintillation layers for X-ray imaging, an X-ray imaging system was employed, as illustrated in Figure 7A. In this system, X-rays generated by an X-ray tube penetrate the object and subsequently irradiate the ceramic scintillator, where the incident X-rays are converted into visible photons. The emitted visible light is then captured by a digital camera and processed to generate the corresponding image. In the experiment, the GAGG: 2 at% Eu^{3+} transparent ceramic scintillator was selected for imaging, as shown in Figure 7B. A capsule containing a miniature spring was used as the imaging target [Figure 7C]. Under a tube voltage of 50 kV, the X-ray intensity was varied by adjusting the tube current from 20 μA to 80 μA. As shown in Figure 7D, both the image brightness and clarity improved with increasing current. At lower currents of 20 μA, the X-ray intensity was insufficient, resulting in a blurred image of the spring. As the current increased, the image quality gradually improved. At 80 μA, the scintillator exhibited the highest imaging brightness, and the internal structure of spring could be clearly distinguished. These preliminary imaging results demonstrate the feasibility of using GAGG: Eu^{3+} transparent ceramics as scintillation converters for X-ray imaging.

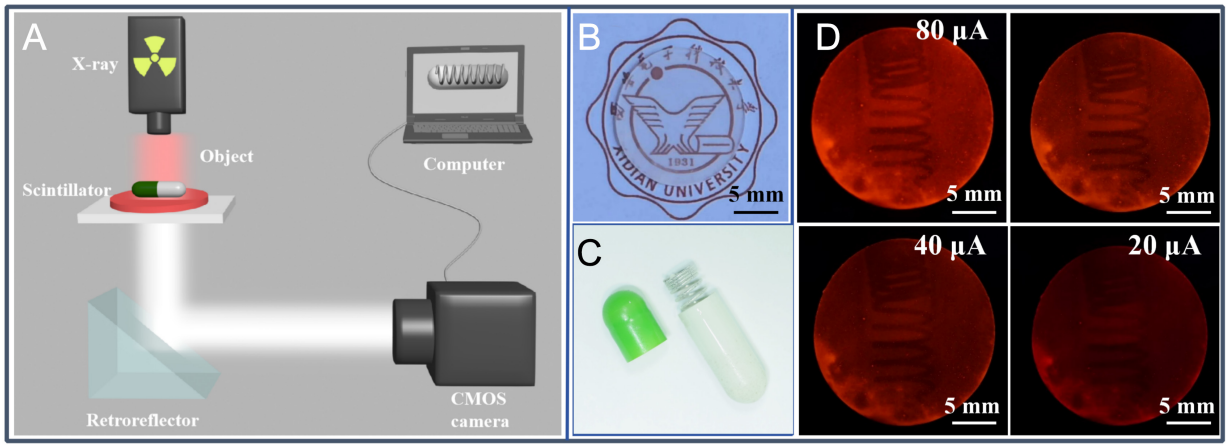

Figure 7. (A) Schematic diagram of the X-ray imaging system; (B) Photograph of GAGG: 2 at% Eu^{3+} ceramic, and (C) photograph of the capsule containing the sub-piece spring under ambient light; (D) X-ray images captured under different X-ray tube currents. GAGG: $Gd_3Al_3Ga_2O_{12}$.

CONCLUSIONS

In summary, a series of GAGG: xEu^{3+} (x = 1~4 at%) transparent ceramic scintillators with narrow-band red emission were successfully fabricated by a solid-state reaction method combined with pressureless sintering. The prepared ceramics exhibited excellent optical properties, with a maximum transmittance of 77% in the 400~800 nm. Photoluminescence investigations demonstrated efficient Eu^{3+} emission and good thermal stability over a wide temperature range. Under X-ray excitation, the GAGG: xEu^{3+} ceramics exhibited intense radioluminescence, and their emission bands exhibited favorable spectral matching with silicon-based photodetectors, indicating their potential for radiation detection applications. The X-ray imaging experiments performed using a self-developed imaging system successfully revealed the internal structure of target objects, highlighting the capability of these ceramic scintillators for X-ray imaging. Overall, the GAGG: Eu^{3+} transparent scintillation ceramics, featuring narrow-band red emission, high transmittance, excellent thermal stability, and effective X-ray imaging performance, represent promising candidates for future applications in X-ray detection and imaging technologies.

DECLARATIONS

Authors' contributions

Conceived and designed the experiment, writing-original draft: Dong, G.; Yang, X.
Performed the experiments and recorded the results: Yang, X.; Bai, R.; Su, H.
Experimental testing and data processing: Yang, X.; Lv, C.; Zhang, B.
Supervision & conceptualization & data curation: Dong, G.; Liu, X.; Wang, T.; Jie, W.

Availability of data and materials

The original contributions presented in this study are included in the article. Further inquiries can be directed to the corresponding author.

AI and AI-assisted tools statement

Not applicable.

Financial support and sponsorship

Supported by the Key Research and Development Program of Shaanxi (2025GH-YBXM-047), the Technology Innovation Leading Program of Shaanxi (2025QCY-KXJ-002), the Fundamental Research Funds for the Central Universities (QTZX26014, ZYTS24120), and the State Key Laboratory of Solidification Processing at NWPU (SKLSP202213).

Conflicts of interest

Dong, G. is a Junior Editorial Board Member of the journal *Microstructures*, but was not involved in any steps of editorial processing, notably including reviewer selection, manuscript handling, and decision-making, while the other authors have declared that they have no conflicts of interest.

Ethical approval and consent to participate

Not applicable.

Consent for publication

Not applicable.

Copyright

REFERENCES

1. Nikl, M.; Yoshikawa, A. Recent R&D trends in inorganic single-crystal scintillator materials for radiation detection. *Adv. Opt. Mater.* **2015**, *3*, 463-81. DOI
2. Ma, J.; Zhu, W.; Lei, L.; et al. Highly efficient $NaGdF_4$:Ce/Tb nanoscintillator with reduced afterglow and light scattering for high-resolution X-ray Imaging. *ACS. Appl. Mater. Interfaces.* **2021**, *13*, 44596-603. DOI
3. Wang, T.; Hu, S.; Ji, T.; et al. High-temperature X-Ray imaging with transparent ceramics scintillators. *Laser. Photonics. Rev.* **2024**, *18*, 2300892. DOI
4. Ou, X.; Qin, X.; Huang, B.; et al. High-resolution X-ray luminescence extension imaging. *Nature* **2021**, *590*, 410-5. DOI
5. Zhu, D.; Nikl, M.; Chewpraditkul, W.; Li, J. Development and prospects of garnet ceramic scintillators: a review. *J. Adv. Ceram.* **2022**, *11*, 1825-48. DOI
6. Kanai, T.; Satoh, M.; Miura, I. Characteristics of a nonstoichiometric $Gd_{3+\delta}(Al,Ga)_{5-\delta}O_{12}$:Ce garnet scintillator. *J. Am. Ceram. Soc.* **2008**, *91*, 456-62. DOI
7. Kuwano, Y.; Saito, S.; Hase, U. Crystal growth and optical properties of Nd: GGAG. *J. Cryst. Growth.* **1988**, *92*, 17-22. DOI
8. Kamada, K.; Endo, T.; Tsutumi, K.; et al. Composition engineering in cerium-doped $(Lu,Gd)_3(Ga,Al)_5O_{12}$ single-crystal scintillators. *Cryst. Growth. Des.* **2011**, *11*, 4484-90. DOI
9. Kamada, K.; Yanagida, T.; Endo, T.; et al. 2Inch diameter single crystal growth and scintillation properties of Ce:$Gd_3Al_2Ga_3O_{12}$. *J. Cryst. Growth.* **2012**, *352*, 88-90. DOI
10. Kunikata, T.; Watanabe, K.; Kantuptim, P.; et al. Dopant concentration dependence on optical and scintillation properties of Eu-doped $Gd_3Al_2Ga_3O_{12}$ single crystals. *Jpn. J. Appl. Phys.* **2024**, *63*, 01SP18. DOI
11. Endo, Y.; Kunikata, T.; Hayashi, N.; et al. Optimization of Al/Ga ratio for light yield of Eu-doped GAGG single-crystal scintillators. *Opt. Mater.* **2026**, *177*, 118181. DOI
12. Lee, G.; Struebing, C.; Wagner, B.; et al. Synthesis and characterization of a $BaGdF_5$:Tb glass ceramic as a nanocomposite scintillator for X-ray imaging. *Nanotechnology* **2016**, *27*, 205203. DOI
13. Zhao, W.; Xu, T.; Wang, Y.; et al. Sintering mechanism and optical properties of $(Lu_{1-x}Sc_xEu_{0.05})_2O_3$ scintillation ceramics. *J. Eur. Ceram. Soc.* **2024**, *44*, 4631-8. DOI
14. Seeley, Z. M.; Cherepy, N. J.; Payne, S. A. Expanded phase stability of Gd-based garnet transparent ceramic scintillators. *J. Mater. Res.* **2014**, *29*, 2332-7. DOI
15. Yanagida, T.; Kamada, K.; Fujimoto, Y.; Yagi, H.; Yanagitani, T. Comparative study of ceramic and single crystal Ce:GAGG scintillator. *Opt. Mater.* **2013**, *35*, 2480-5. DOI
16. Wu, Y.; Luo, Z.; Jiang, H.; Meng, F.; Koschan, M.; Melcher, C. L. Single crystal and optical ceramic multicomponent garnet scintillators: a comparative study. *Nucl. Instrum. Methods. Phys. Res. Sect. A.* **2015**, *780*, 45-50. DOI
17. Drdlikova, K.; Klement, R.; Hadraba, H.; Drdlik, D.; Galusek, D.; Maca, K. Luminescent Eu^{3+}-doped transparent alumina ceramics with high hardness. *J. Eur. Ceram. Soc.* **2017**, *37*, 4271-7. DOI
18. Zhang, C.; Shi, Y.; Wang, X.; Qi, J.; Lu, T. Mechanical, photoluminescent properties and energy transfer mechanism of highly transparent $(Y_{0.99-x}Gd_xSm_{0.01})_2O_3$ ceramics for scintillator applications. *J. Eur. Ceram. Soc.* **2024**, *44*, 1783-94. DOI
19. Liu, Y.; Liu, S.; Sun, P.; et al. Transparent ceramics enabling high luminous flux and efficacy for the next-generation high-power LED light. *ACS. Appl. Mater. Interfaces.* **2019**, *11*, 21697-701. DOI
20. Liu, S.; Sun, P.; Liu, Y.; et al. Warm white light with a high color-rendering index from a single $Gd_3Al_4GaO_{12}:Ce^{3+}$ transparent ceramic for high-power LEDs and LDs. *ACS. Appl. Mater. Interfaces.* **2019**, *11*, 2130-9. DOI

21. Dimitrakopoulos, A.; Michail, C.; Valais, I.; Fountos, G.; Kandarakis, I.; Kalyvas, N. Experimental evaluation of GAGG:Ce crystalline scintillator properties under X-ray radiation. *Crystals* **2025**, *15*, 590. DOI
22. Rodríguez-garcía, M. M.; Ciric, A.; Ristic, Z.; Williams, J. A. G.; Dramićanin, M. D.; Evans, I. R. Narrow-band red phosphors of high colour purity based on Eu^{3+}-activated apatite-type $Gd_{9.33}(SiO_4)_6O_2$. *J. Mater. Chem. C.* **2021**, *9*, 7474-84. DOI
23. Hora, D. A.; Andrade, A. B.; Ferreira, N. S.; Teixeira, V. C.; dos S. Rezende, M. V. Effect of the PVA (polyvinyl alcohol) concentration on the optical properties of Eu-doped YAG phosphors. *Opt. Mater.* **2016**, *60*, 495-500. DOI
24. Xu, J.; Ueda, J.; Tanabe, S. Design of deep-red persistent phosphors of $Gd_3Al_{5-x}Ga_xO_{12}:Cr^{3+}$ transparent ceramics sensitized by Eu^{3+} as an electron trap using conduction band engineering. *Opt. Mater. Express.* **2015**, *5*, 963. DOI
25. Gerasymov, I.; Nepokupnaya, T.; Boyarintsev, A.; et al. GAGG:Ce composite scintillator for X-ray imaging. *Opt. Mater.* **2020**, *109*, 110305. DOI
26. Toby, B. H.; Von Dreele, R. B. *GSAS-II*: the genesis of a modern open-source all purpose crystallography software package. *J. Appl. Cryst.* **2013**, *46*, 544-9. DOI
27. Hua, H.; Feng, S.; Ouyang, Z.; et al. YAGG:Ce transparent ceramics with high luminous efficiency for solid-state lighting application. *J. Adv. Ceram.* **2019**, *8*, 389-98. DOI
28. Korzhik, M.; Borisevich, A.; Fedorov, A.; et al. The scintillation mechanisms in Ce and Tb doped $(Gd_xY_{1-x})Al_2Ga_3O_{12}$ quaternary garnet structure crystalline ceramics. *J. Lumin.* **2021**, *234*, 117933. DOI
29. Feng, G.; Wu, Y.; Lu, H.; Zhang, R.; Wang, S.; Wu, S. Eu-doped $(Y_{0.85-x}La_{0.15})_2O_3$ sesquioxide transparent ceramics for high-spatial-resolution X-ray imaging. *J. Mater. Chem. C.* **2023**, *11*, 2863-70. DOI
30. Otsuka, T.; Oka, R.; Hayakawa, T. Eu^{3+} site distribution and local distortion of photoluminescent $Ca_3WO_6:(Eu^{3+}, K^+)$ double perovskites as high-color-purity red phosphors. *Adv. Sci.* **2023**, *10*, e2302559. DOI PubMed PMC
31. Wang, Y.; Ke, Y.; Chen, S.; et al. Luminescence investigation of red-emitting $Sr_2MgMoO_6:Eu^{3+}$ phosphor for visualization of latent fingerprint. *J. Colloid. Interface. Sci.* **2021**, *583*, 89-99. DOI
32. Xu, D.; Zhou, W.; Zhang, Z.; Ma, X.; Xia, Z. Luminescence property and energy transfer behavior of apatite-type $Ca_4La_6(SiO_4)_4(PO_4)_2O_2:Tb^{3+}$, Eu^{3+} phosphor. *Mater. Res. Bull.* **2018**, *108*, 101-5. DOI
33. Li, M.; Jiao, B. Synthesis and photoluminescence properties of $ZnTiO_3:Eu^{3+}$ red phosphors via sol-gel method. *J. Rare. Earths.* **2015**, *33*, 231-8. DOI
34. Mhlongo, G.; Dhlamini, M.; Swart, H.; Ntwaeaborwa, O.; Hillie, K. Dependence of photoluminescence (PL) emission intensity on Eu^{3+} and ZnO concentrations in $Y_2O_3:Eu^{3+}$ and $ZnO{\cdot}Y_2O_3:Eu^{3+}$ nanophosphors. *Opt. Mater.* **2011**, *33*, 1495-9. DOI
35. Xia, L.; Hu, T.; Liu, H.; et al. B-site Y^{3+} assisted charge compensation strategy to synthesize Eu^{3+} doped ruddlesden-popper Ca_2SnO_4 perovskite and photoluminescence properties. *J. Alloys. Compd.* **2020**, *845*, 156131. DOI
36. Blasse, G. Energy transfer between inequivalent Eu^{2+} ions. *J. Solid. State. Chem.* **1986**, *62*, 207-11. DOI
37. Kunti, A. K.; Patra, N.; Harris, R. A.; et al. Structural properties and luminescence dynamics of $CaZrO_3:Eu^{3+}$ phosphors. *Inorg. Chem. Front.* **2021**, *8*, 821-36. DOI
38. Dexter, D. L. A theory of sensitized luminescence in solids. *J. Chem. Phys.* **1953**, *21*, 836-50. DOI
39. Fu, A.; Pang, Q.; Yang, H.; Zhou, L. $Ba_2YNbO_6:Mn^{4+}$ -based red phosphor for warm white light-emitting diodes (WLEDs): photoluminescent and thermal characteristics. *Opt. Mater.* **2017**, *70*, 144-52. DOI
40. Shisina, S.; Das, S.; Som, S.; et al. Structure and optoelectronic properties of palmierite structured $Ba_2Y_{0.67}\delta_{0.33}V_2O_8:Eu^{3+}$ red phosphors for n-UV and blue diode based warm white light systems. *J. Alloys. Compd.* **2019**, *802*, 723-32. DOI
41. Naresh, V.; Cha, P. R.; Lee, N. $Cs_2NaGdCl_6:Tb^{3+}$-a highly luminescent rare-earth double perovskite scintillator for low-dose X-ray detection and imaging. *ACS. Appl. Mater. Interfaces.* **2024**, *16*, 19068-80. DOI PubMed
42. Chen, Y.; Zeng, R.; Wei, Q.; et al. Competing energy transfer-modulated dual emission in Mn^{2+}-doped $Cs_2NaTbCl_6$ rare-earth double perovskites. *J. Phys. Chem. Lett.* **2022**, *13*, 8529-36. DOI
43. Long, J.; Yang, C.; Li, B.; Ma, R.; Huang, W. Novel orange-red emitting phosphor $Y_2MgTiO_6:Sm^{3+}$ luminescence properties and optical thermometry. *Ceram. Int.* **2024**, *50*, 19325-34. DOI
44. Cui, R.; Zhao, R.; Yu, P.; Gong, X.; Deng, C.; Zhang, J. A novel red phosphor $Sr_3In_2WO_9$: Eu^{3+} for WLEDs. *Inorg. Chem. Commun.* **2023**, *157*, 111410. DOI
45. Zhang, S.; Zhao, F.; Liu, S.; Song, Z.; Liu, Q. An improved method to evaluate trap depth from thermoluminescence. *J. Rare. Earths.* **2025**, *43*, 262-9. DOI

46. Zhang, Q.; Ding, X.; Ma, X.; Su, Z.; Liu, B.; Wang, Y. Highly efficient and thermally stable broadband NIR phosphors with superlong afterglow performance and their multifunctional applications. *Laser. Photonics. Rev.* **2024**, *18*, 2400541. DOI